

# Tracking Anything in Heart All at Once

Chengkang Shen, Hao Zhu, You Zhou, Yu Liu, Si Yi, Lili Dong, Weipeng Zhao, David J. Brady, Xun Cao, Zhan Ma, and Yi Lin

**Abstract**—Myocardial motion tracking stands as an essential clinical tool in the prevention and detection of Cardiovascular Diseases (CVDs), the foremost cause of death globally. However, current techniques suffer incomplete and inaccurate motion estimation of the myocardium both in spatial and temporal dimensions, hindering the early identification of myocardial dysfunction. In addressing these challenges, this paper introduces the Neural Cardiac Motion Field (NeuralCMF). NeuralCMF leverages the implicit neural representation (INR) to model the 3D structure and the comprehensive 6D forward/backward motion of the heart. This approach offers memory-efficient storage and continuous capability to query the precise shape and motion of the myocardium throughout the cardiac cycle at any specific point. Notably, NeuralCMF operates without the need for paired datasets, and its optimization is self-supervised through the physics knowledge priors both in space and time dimensions, ensuring compatibility with both 2D and 3D echocardiogram video inputs. Experimental validations across three representative datasets support the robustness and innovative nature of the NeuralCMF, marking significant advantages over existing state-of-the-arts in cardiac imaging and motion tracking.

**Index Terms**—Myocardial motion tracking, Echocardiogram videos, Implicit neural representation, Cardiac imaging

## I. INTRODUCTION

CARDIOVASCULAR Diseases (CVDs) stand as the primary global cause of death [1]. While CVDs encompass a spectrum of pathological disorders, including coronary atherosclerosis, valvular insufficiency, and inflammatory myocarditis, each impairs the heart's motion and pumping function [2]. Therefore, accurate tracking of myocardial motion

This work was supported by the NSFC (No. 62022038, 62101242, 62071219, 62025108, U20A20184) and the Science and Technology Commission of Shanghai Municipality (STCSM) (No. 20Y11909800).

Chengkang Shen, Hao Zhu, You Zhou, Si Yi, Xun Cao and Zhan Ma are with the School of Electronic Science and Engineering, Nanjing University, Nanjing, 210023, China.

You Zhou is also with the Medical School, Nanjing University, Nanjing, 210093, China.

Yu Liu, Lili Dong and Weipeng Zhao are with the Department of Echocardiography of Zhongshan Hospital, Fudan University, Shanghai, 200032, China.

David J. Brady is with the College of Optical Sciences, University of Arizona, Tucson, AZ 85721, USA.

Yi Lin is with the Department of Cardiovascular Surgery of Zhongshan Hospital, Fudan University, Shanghai, 200032, China.

Chengkang Shen, Hao Zhu and You Zhou contributed equally to this work.

Corresponding authors: Yi Lin, Zhan Ma, and Xun Cao. (e-mail: lyricist2012@163.com; mazhan@nju.edu.cn; caoxun@nju.edu.cn)

This work has been submitted to the IEEE for possible publication. Copyright may be transferred without notice, after which this version may no longer be accessible.

is pivotal for detecting CVDs, emphasizing the importance of accurate myocardial motion tracking. Currently, two primary modalities for myocardial motion tracking exist, namely echocardiography and cardiac magnetic resonance (CMR). Considering factors such as economics, prevalence, operational complexity, and temporal resolution, echocardiography is favored over CMR [3]–[5]. Consequently, developing and implementing an accurate and robust 3D myocardial motion tracking method based on echocardiography is critical in modern cardiology practice.

While numerous methods have been proposed to track myocardial motion in echocardiogram videos, several challenges persist in existing solutions. In speckle-based tracking approaches [5]–[8] which aim to identify consistent intensity patterns across successive frames by optimizing their similarities, capturing motion trajectories over extended temporal frames remains a formidable task due to the inherent limitation of estimating motions frame by frame. Surface-based tracking techniques [9]–[14], on the other hand, concentrate on capturing similar curvature or shape characteristics of the chamber's boundaries across sequential frames. However, the necessity for interpolating motion vectors for points within the boundary introduces inaccuracies, particularly in myocardium regions that are not fully infarcted. For instance, in cases of cardiac sarcoidosis [15], [16], where motion across the entire myocardium lacks uniformity. More recently, deep learning-based tracking methods have achieved remarkable success in analyzing deformations between images [17]–[19]. However, they face limitations in predicting the complete cardiac cycle's motion and suffer from the unavailability of large-scale paired datasets. In summary, current myocardial motion tracking techniques with echocardiogram videos input encounter three primary challenges: (1) *accurate and complete estimation of myocardial motion throughout the entire cardiac cycle*, (2) *tracking any points in the 3D heart without resorting to interpolation*, and (3) *operating without the need for additional paired training datasets*.

In this manuscript, we present Neural Cardiac Motion Field (NeuralCMF), an innovative self-supervised technique designed to simultaneously model the 3D cardiac structure and capture the 6D forward/backward motions of the myocardium. In contrast to prior methods that primarily focus on comparing neighbouring frames pairwise, NeuralCMF takes a unique approach by modeling the global motion of all pixels throughout the entire video as a continuous implicit neural function, which has a coordinate input and the corresponding shape/motion output. Consequently, this enables us to precisely query the motion trajectory for any pixel spanning the complete cardiac

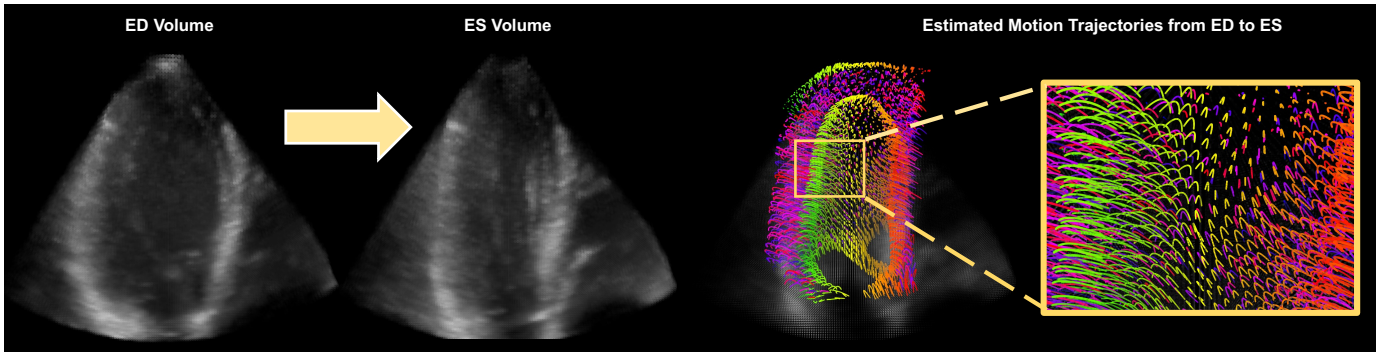


Fig. 1. We introduce a self-supervised method for estimating 3D motion trajectories throughout the cardiac cycle at any given point all at once. The figure illustrates the motion estimation of the 3D heart from end-diastole (ED) to end-systole (ES), representing the heart's contraction phase. The estimated motion trajectories are displayed on the right with each point's trajectory depicted in a different color for clarity. Though we have chosen to show only sparse trajectories of the left ventricular (LV) myocardium, our method has the ability to compute motion for all points across the entire 3D heart.

cycle, as demonstrated in Fig. 1. Rather than depending on the extensive paired dataset for supervision, NeuralCMF employs a physics-informed self-supervision mechanism. This mechanism involves comparing the loss between the network output after physical imaging operators and the input videos during optimization (see Fig. 2). As a result, NeuralCMF effectively eliminates the dataset dependency commonly found in current deep learning-based methods. Furthermore, as the physical imaging operators could be modified according to 2D/3D echocardiogram videos, NeuralCMF could be seamlessly integrated with both 2D and 3D echocardiogram videos inputs. To the best of our knowledge, this universality for estimating 3D myocardial motion using echocardiogram videos from both 2D and 3D sources is firstly achieved in the community. The quantitative and qualitative experiments conducted on three representative datasets, spanning both 2D and 3D echocardiogram videos, show that the performance of our approach consistently outperforms the existing state-of-the-art methods [19], [20]. We believe the methodology presented here may also be applicable across more imaging modalities beyond ultrasonic imaging for analyzing the motion of organs other than the heart.

The contributions of this paper are summarized below:

- We present NeuralCMF, a novel self-supervised method that simultaneously models the 3D structure of the heart and 6D forward/backward motion of the myocardium.
- NeuralCMF can estimate the 3D motion of any specific point in the heart throughout the cardiac cycle by interpreting echocardiogram videos, irrespective of their resolution or whether they are in 2D or 3D format.
- NeuralCMF provides state-of-the-art performance in quantitative and qualitative assessments when tested on three separate datasets.

## II. RELATED WORK

### A. Cardiac Motion Tracking Methods

Motion tracking is crucial for precise strain calculations, and its objective is to map the displacement between consecutive images in a sequence. This section reviews existing motion tracking algorithms.

1) *Intensity-based Methods*: Speckle-tracking methods identify consistent intensity patterns across several consecutive time frames by maximizing the similarity of these patterns [7], [8]. These algorithms operate under the premise that there is only a small displacement motion between frames and that the intensity of a specific point within a moving object will remain unchanged. Nevertheless, the precision of speckle tracking tends to diminish when the temporal intervals between frames become substantial.

2) *Feature-based Methods*: Feature-based algorithms utilize image attributes such as surfaces, texture, or curvature, allowing consistent tracking over time [9], [11], [13]. These methods generate motion fields by matching the key points across frames based on features. The point matching algorithms include iterative closest point matching [21] and robust point matching [22]. Although efficient, these approaches are limited by the dependency on accurate segmentation and often produce sparse motion fields that need additional interpolation to generate motion in the desired locations.

3) *Deep Learning-based Methods*: State-of-the-art methods are driven by deep learning, gaining traction for their computational efficiency and pattern recognition capabilities. In the realm of supervised learning, a variety of methods have emerged: Rohé *et al.* [23] developed a method that leveraged a convolutional neural network (CNN) guided by the mesh segmentation of paired images to compute transformations between pairs of CMR images. Parajuli *et al.* [10] introduced the Flow Network Tracker (FNT), employing a convolutional autoencoder to extract a point cloud from myocardium segmentation, followed by point tracking across time frames. Wu *et al.* [24] utilized a deep Boltzmann machine (DBM) to capture both local and global heart shape variations, enabling frame-by-frame heart motion tracking in CMR images. However, these supervised methodologies predominantly rely on simulated datasets with known ground-truth deformations or expert-labeled myocardium segmentations, which are difficult to collect in real cases.

Limited ground truth motion labels have increased interest in unsupervised motion tracking. This has led to the evolution of methods employing diverse U-Net architectures [25] for cardiac motion tracking [17], [26], [27]. However, these methods have mostly been limited to the analysis of 2D heart images or CMR images, leaving motion tracking on 3D

echocardiography an enduring challenge. Recent works, such as Ta *et al.* [18] with a proposed semi-supervised joint network and Ahn *et al.* [19] with a co-attention spatial transformer network, both for pairs of 3D heart images motion estimation, have shown promising advancements. Yet, these approaches remain limited in concurrently predicting the entire cardiac cycle's motion, necessitating extensive training datasets and exhibiting susceptibility to data bias.

Deep learning-based methods have shown significant promise in cardiac motion tracking. Nonetheless, no methods can predict complete myocardial motion throughout the cardiac cycle without relying on simulated or expert-labeled datasets, a factor that is critical for clinical use.

### B. Implicit Neural Representation

The implicit neural representation (INR) [28], which is also called as the neural fields [29], characterizes the function of a signal by mapping the coordinate to its attribute using a neural network. Different from previous deep-learning techniques [30] which is supervised by a large-scale paired dataset, the training of INR follows a self-supervised mechanism. This self-supervised mechanism could be embedded with various differentiable physics operators, making the INR naturally suitable for solving domain-specific inverse problems where the large-scale paired dataset is unavailable. As a result, INR has been widely applied in various tasks, such as the neural rendering [29], [31], microscopy imaging [32], [33], material design [34] and partial differential equations solver [35].

Recently, INR has gained prominence in medical imaging. Focusing on the realm of 2D/3D image reconstruction, the prevalent modalities such as Computed Tomography (CT), Magnetic Resonance Imaging (MRI), and ultrasound have seen numerous advancements. For instance, in the context of CT image reconstruction, Shen *et al.* [36] introduced a method that used prior images and INR to reconstruct high-quality 2D CT images from sparse samples. Zha *et al.* [37] proposed a method for sparse-view Cone Beam Computed Tomography (CBCT) reconstruction, using INR to model the attenuation field and optimize it by minimizing discrepancies between actual and synthesized projections. In the MRI reconstruction realm, Wu *et al.* [38] used high and low-resolution MRI image pairs to represent the 3D brain surface, processed the low-resolution images with a super-resolution CNN, and combined the extracted features with high-resolution coordinates in an MLP decoder to determine 3D voxel intensity. For ultrasound reconstruction, Shen *et al.* [39] proposed CardiacField to produce a high-fidelity 3D heart and automatically estimate heart function using only low-cost two-dimensional echocardiography (2DE) probes.

While numerous methods have employed INR to address challenges in medical imaging, none have explored its application for cardiac motion analysis in ultrasound modality, which is paramount in the clinical assessment of cardiac function.

## III. METHODOLOGY

### A. Overview

Aligned with our aim to attain a comprehensive understanding of cardiac dynamics, we present a self-supervised

methodology that utilizes INR to accurately estimate the 3D motion of the myocardium throughout the entire cardiac cycle. The method is applicable to both 2D and 3D echocardiogram videos. As depicted in Fig. 2, the inputs of our method are the 4D space-time coordinates  $(x, y, z, t)$  in the heart. The corresponding outputs consist of the intensity value  $O(x, y, z, t)$  at the specified space-time location, along with the forward and backward motion vectors  $\vec{M} = \{\vec{m}_{t \rightarrow t+1}, \vec{m}_{t \rightarrow t-1}\}$  of the location  $(x, y, z, t)$  at successive time frames  $t + 1$  and  $t - 1$ , respectively.

Our approach extends our previous work, CardiacField [39], by integrating the temporal dimension into the network input, enabling quantify the motion of the myocardium throughout the entire cardiac cycle. In the following sections, we will begin by briefly reviewing the core of the CardiacField [39]. Subsequently, we will detail the NeuralCMF and its optimization strategy.

### B. Background

Our previous study, CardiacField [39], focuses on reconstructing the 3D heart from a 2D echocardiogram video captured from different angles. To achieve this, it represents a static 3D heart as a continuous function using the INR, denoted by  $F_{\theta}^{static}$ . This function takes 3D positions  $\vec{X} = (x, y, z)$  as input and yields the corresponding volume intensity  $O(\vec{X})$ ,

$$O(\vec{X}) = F_{\theta}^{static}(\vec{X}), \quad (1)$$

where the function  $F_{\theta}^{static}$  is modelled using a multi-resolution hash-based MLP network [40], [41]. To supervise the training of the network parameters in CardiacField [39], the physical imaging process of 2D echocardiographic images is introduced to construct the physics-informed loss function. In detail, each 2D image could be viewed as applying a virtual slicing operation to the 3D cardiac volume according to the angles of different images, *i.e.*,

$$\mathbf{I}_s = \mathcal{S}_2^3 \circ \mathcal{B} \circ O(\vec{X}), \quad (2)$$

where  $\mathcal{S}_M^N$  is the slicing operator that reduces an  $N$ -dimensional function down to an  $M$ -dimensional one by zeroing out the last  $N - M$  dimensions.  $\mathcal{B}$  characterizes the angle of different images and is used to transform the coordinates from the global world coordinate system to the image plane system. Subsequently, the 2D images  $\mathbf{I}_s$  derived from  $O(\vec{X})$ , are compared to different frames  $\mathbf{I}_g$  in the input 2D echocardiogram video using a mean squared error loss,

$$\mathcal{L}_{CardiacField} = \frac{1}{K} \sum_i^K \|\mathbf{I}_s^i - \mathbf{I}_g^i\|_2^2, \quad (3)$$

where  $K$  refers to the number of frames in the input 2D echocardiogram video,  $\mathbf{I}_g^i$  is the  $i$ -th image in the input video,  $\|\cdot\|_2$  denotes the  $L_2$ -norm of the vector or matrix  $\cdot$ . Finally, the loss  $\mathcal{L}_{CardiacField}$  is used to update the network parameters  $\theta$  in  $F_{\theta}^{static}$  and the angle parameters in  $\mathcal{B}$  following the backward gradient flow. Once the training of  $F_{\theta}^{static}$  is converged, the 3D structure of the heart could be reconstructed by feeding the coordinate  $\vec{X}$  to the  $F_{\theta}^{static}$  one by one. As a result, CardiacField could be used to reconstruct the 3D heart

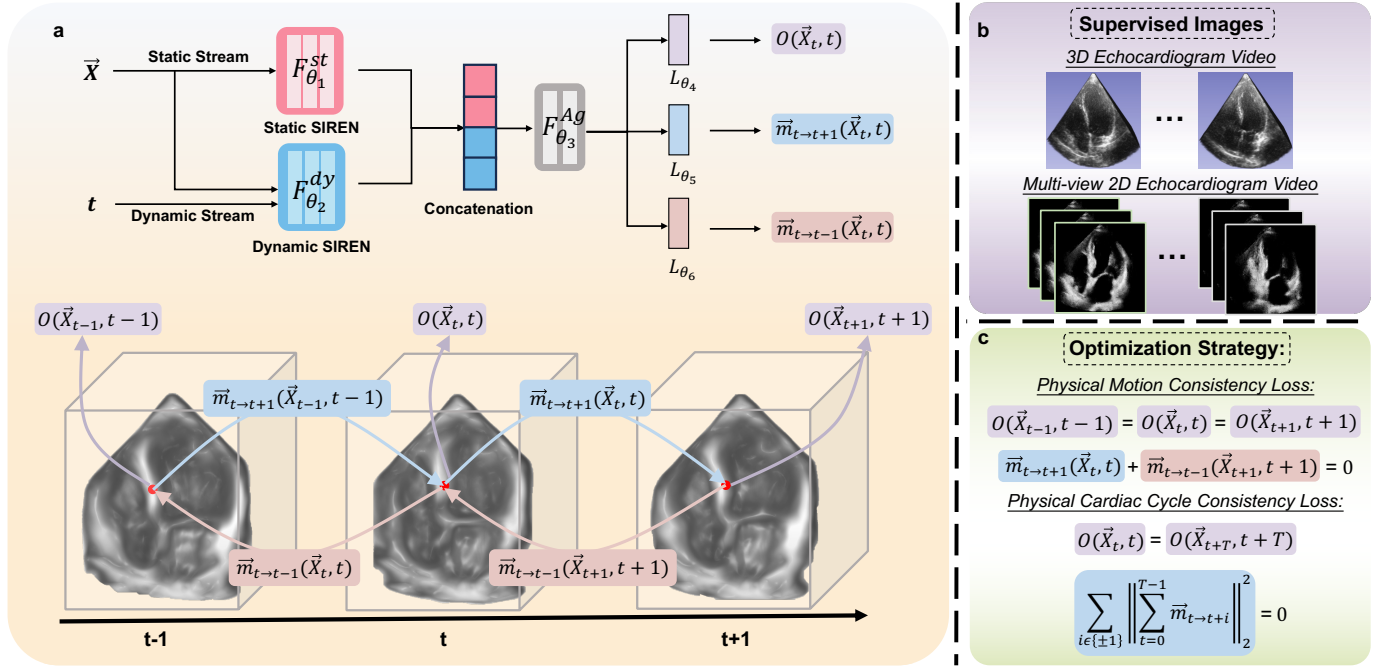


**Fig. 2.** The figure illustrates the workflow of our method. (a) Inputs consist of 4D space-time coordinates  $(x, y, z, t)$ . Corresponding outputs include the intensity value  $O(x, y, z, t)$  at specified space-time locations, as well as forward and backward 3D motion vectors  $\vec{M} = (\vec{m}_{t \rightarrow t+1}, \vec{m}_{t \rightarrow t-1})$  that represent the movements of  $(x, y, z)$  at successive time frames  $t+1$  and  $t-1$ , respectively. (b) Our approach can be applied to both 2D and 3D echocardiogram videos. (c) The methodology utilizes two main optimization strategies: physical motion consistency loss, ensuring that intensity remains constant within both the heart's tissues and blood-filled areas throughout the entire cardiac cycle, and physical cardiac cycle consistency loss, which aligns the process with the physiological fact that the heart muscle returns to its initial shape upon completing one full cardiac cycle.

from 2D echocardiogram video without attaching any other position sensors.

### C. Neural Cardiac Motion Field

In order to quantify the deformation of the myocardium, we extend the static 3D heart representation in CardiacField [39] to dynamic reconstruction and formulate the dense 3D motion field of the myocardium using the INR. Given a 3D position  $\vec{X}$  at a specific time  $t$ , our model  $F_{\theta}^{Motion}$  predicts not only the volume intensity  $O(\vec{X}, t)$  but also the forward and backward motion vectors. These vectors are expressed as  $\vec{M}(\vec{X}, t) = \{\vec{m}_{t \rightarrow t+1}(\vec{X}, t), \vec{m}_{t \rightarrow t-1}(\vec{X}, t)\}$ , representing the 3D offset vectors of  $\vec{X}$  between consecutive time frames  $t$  to  $t+1$  and  $t$  to  $t-1$ . Accordingly, the dynamic model is mathematically defined as follows,

$$\{O(\vec{X}, t), \vec{M}(\vec{X}, t)\} = F_{\theta}^{Motion}(\vec{X}, t). \quad (4)$$

As depicted in Fig. 2, the network  $F_{\theta}^{Motion}$  consists of a static and dynamic stream. The static stream takes the 3D position vector  $\vec{X}$  as its input, while the dynamic stream's input consists of the concatenation of the 3D position vector  $\vec{X}$  and time  $t$ . The networks within the static  $F_{\theta_1}^{st}$  and dynamic  $F_{\theta_2}^{dy}$  streams are formulated using the SIREN network [28]. Each network has 4 layers, with 64 neurons in each hidden layer. The outputs of the two streams are static and dynamic feature vectors with length 32, respectively. The static feature vector captures the heart's shape in the first frame. The dynamic feature vectors are essential to capture the transient changes of the myocardium that occur over time. These

feature vectors are then concatenated and fed into a feature aggregation network  $F_{\theta_3}^{Ag}$ , comprising a single layer with 64 neurons. The output of the feature aggregation network is further fed into three distinct layers ( $L_{\theta_4}$ ,  $L_{\theta_5}$ , and  $L_{\theta_6}$ ) to obtain the volume intensity  $O(\vec{X}, t)$  and 3D motion vectors  $\vec{m}_{t \rightarrow t+1}(\vec{X}, t)$  and  $\vec{m}_{t \rightarrow t-1}(\vec{X}, t)$ ,

$$\begin{aligned} \mathbf{H} &= F_{\theta_3}^{Ag}(\text{Concat}(F_{\theta_1}^{st}(\vec{X}), F_{\theta_2}^{dy}(\vec{X}, t))) \\ O(\vec{X}, t) &= \sigma(L_{\theta_4}(\mathbf{H})) \\ \vec{m}_{t \rightarrow t+1}(\vec{X}, t) &= \tanh(L_{\theta_5}(\mathbf{H})) \\ \vec{m}_{t \rightarrow t-1}(\vec{X}, t) &= \tanh(L_{\theta_6}(\mathbf{H})) \end{aligned} \quad (5)$$

where  $\theta_i$  denotes the parameters of the corresponding neural network.  $\sigma$  and  $\tanh$  refer to the Sigmoid and Tanh activation functions, respectively.

### D. Physics-informed Optimization

To supervise the training of the network parameters, a physics-informed loss function is proposed,

$$\mathcal{L} = \underbrace{\mathcal{L}_{imag}}_{\text{Static Prior}} + \underbrace{\mathcal{L}_{motion} + \mathcal{L}_{cycle}}_{\text{Motion Prior}} + \alpha_r \mathcal{L}_{reg} \quad (6)$$

where  $\mathcal{L}_{imag}$  and  $\mathcal{L}_{motion}$ ,  $\mathcal{L}_{cycle}$  respectively model the static and dynamic physical knowledge priors,  $\mathcal{L}_{reg}$  regularizes the loss function. The term  $\alpha_r$  represents the weight of the regularization loss. Subsequent sections will provide a detailed elaboration of different components in the loss function.

1) **Physical Imaging loss:** The physical imaging loss focuses on modeling the static 3D structure information in NeuralCMF according to the input echocardiogram videos. Because the physical imaging process of the three-dimensional echocardiography (3DE) varies from the 2DE, the formula for  $\mathcal{L}$  varies accordingly:

$$\mathcal{L}_{imag} = \begin{cases} \sum_{t=0}^{T-1} \sum_{X_t} \left\| O(\vec{X}_t, t) - \mathbf{I}_g(\vec{X}_t, t) \right\|_2^2 & \text{3D Echo.} \\ \mathcal{L}_{CardiacField} \text{ (Eqn. 3)} & \text{2D Echo.} \end{cases}, \quad (7)$$

where  $\mathbf{I}_g$  refers to the input 3D or 2D echocardiogram videos,  $\vec{X}_t$  is a 3D point at time  $t$  and its definition domain is determined by the resolution of input videos, *e.g.*,  $\vec{X}_t \in \{0, 1, \dots, 159\}^3$  for a input 3D video with resolution  $160^3$ . When a 3D echocardiogram video is given, the 3D structure of the heart could be supervised directly by comparing the network output  $O(\vec{X}_t, t)$  with the input video. However, when a 2D video is given, the slicing operation (Eqn. 2) in 2D echocardiography should be involved to generate a 2D image for comparing with the input 2D image. Note that the parameters for characterizing the angles of different 2D images are also optimized automatically in the training process.

2) **Physical Motion Consistency Loss:** In echocardiogram videos, the intensity remains consistent in both the heart's tissues and blood-filled areas throughout the entire cardiac cycle [42]. Taking inspiration from this 'consistent intensity' prior, we propose the physical motion consistency loss, ensuring the continuity of intensity for any given point within the 3D heart over time. Given a point  $\vec{X}$  in the 3D heart at time  $t$ , *i.e.*,  $\vec{X}_t$ , its corresponding point at time  $t+1$  and  $t-1$  could be calculated by,

$$\begin{aligned} \vec{X}_{t+1} &= \vec{X}_t + \vec{m}_{t \rightarrow t+1}(\vec{X}_t, t) \\ \vec{X}_{t-1} &= \vec{X}_t + \vec{m}_{t \rightarrow t-1}(\vec{X}_t, t). \end{aligned} \quad (8)$$

Then, these new positions are fed into the  $F_{\theta}^{Motion}$  to obtain the corresponding intensity values, forward and backward motions. Following the 'consistent intensity' prior, the physical motion consistency loss could be mathematically modelled as follows,

$$\begin{aligned} \mathcal{L}_{motion} &= \sum_{t=0}^{T-1} \sum_{\vec{X}_t} \sum_{i \in \{\pm 1\}} \left( \left\| O(\vec{X}_{t+i}, t+i) - O(\vec{X}_t, t) \right\|_2^2 \right. \\ &\quad \left. + \alpha_1 \left\| \vec{X}_{t+i} + \vec{m}_{t \rightarrow t-i}(\vec{X}_{t+i}, t+i) - \vec{X}_t \right\|_2^2 \right), \end{aligned} \quad (9)$$

where  $T$  denotes the total frames in an entire cardiac cycle.

3) **Physical Cardiac Cycle Consistency Loss:** To enhance the precision of our model and align it with the physiological realities of cardiac function, we incorporate a physical cardiac cycle consistency loss. This loss reflects the fundamental cyclical behavior of cardiac motion throughout a single heart cycle, recognizing that the heart muscle returns to its initial shape after completing one cardiac cycle. The cycle consistency involves two primary constraints,

- **Intensity constraint.** The intensity of a particular point at the end of a cardiac cycle should closely align with its intensity at the beginning of the cycle. This intensity consistency condition reinforces the model's alignment with physical principles, ensuring the intensity is consistent across a full cycle.
- **Motion constraint.** The heart's cyclic motion dictates that the cumulative forward or backward motions over the course of one cardiac cycle should sum to zero. This constraint ensures that the cardiac model adheres to the biological principle that the heart returns to its original shape after a complete cycle.

Mathematically, these two constraints could be formulated as,

$$\begin{aligned} \mathcal{L}_{cycle} &= \sum_{\vec{X}_t} \left\| O(\vec{X}_{t+T}, t+T) - O(\vec{X}_t, t) \right\|_2^2 \\ &\quad + \alpha_2 \sum_{i \in \{\pm 1\}} \left\| \sum_{t=0}^{T-1} \vec{m}_{t \rightarrow t+i} \right\|_2^2. \end{aligned} \quad (10)$$

4) **Regularization Loss:** To reduce the noisy mismatch caused by the low signal-to-noise ratio in the input echocardiogram videos, two regularization terms are introduced in our model. The first term enforces consistency between the predicted forward and backward 3D motion vectors at each time step, ensuring that the forward motion vector  $\vec{m}_{t \rightarrow t+1}(\vec{X}_t, t)$ , is congruent with the corresponding backward motion vector,  $\vec{m}_{t \rightarrow t-1}(\vec{X}_t, t)$ . The second term serves to minimize the magnitude of the 3D motion vectors at each time step, promoting smoothness in the modeled motion. The regularization loss is thus formulated as follows,

$$\begin{aligned} \mathcal{L}_{reg} &= \sum_{t=0}^{T-1} \sum_{\vec{X}_t} \left( \left\| \vec{m}_{t \rightarrow t+1}(\vec{X}_t, t) + \vec{m}_{t \rightarrow t-1}(\vec{X}_t, t) \right\|_1 \right. \\ &\quad \left. + \left\| \vec{m}_{t \rightarrow t+1}(\vec{X}_t, t) \right\|_1 + \left\| \vec{m}_{t \rightarrow t-1}(\vec{X}_t, t) \right\|_1 \right). \end{aligned} \quad (11)$$

## IV. EXPERIMENTS

### A. Datasets

We employ three distinct echocardiogram video datasets to evaluate the proposed NeuralCMF, each contributing unique characteristics and challenges.

1) **STRAUS Datasets:** The open-source 3D Strain Assessment in Ultrasound (STRAUS) dataset [43] consists of 8 distinct volumetric sequences, each corresponding to a specific physiological condition. These include one healthy sequence, four ischemic cases, and three simulations of dilated cardiomyopathy. The ischemic cases are characterized by occlusions in various coronary arteries: the proximal or distal parts of the left anterior descending coronary artery (LADprox and LADdist, respectively), the left circumflex coronary artery (LCX), and the right coronary artery (RCA). The simulations of dilated cardiomyopathy consist of one case with a synchronous activation pattern (sync) and two cases of dyssynchrony due to left branch bundle block (LBBBsmall and LBBBlarge). These dyssynchronous cases are further distinguished by a progressively longer delay in activating the septum and lateral

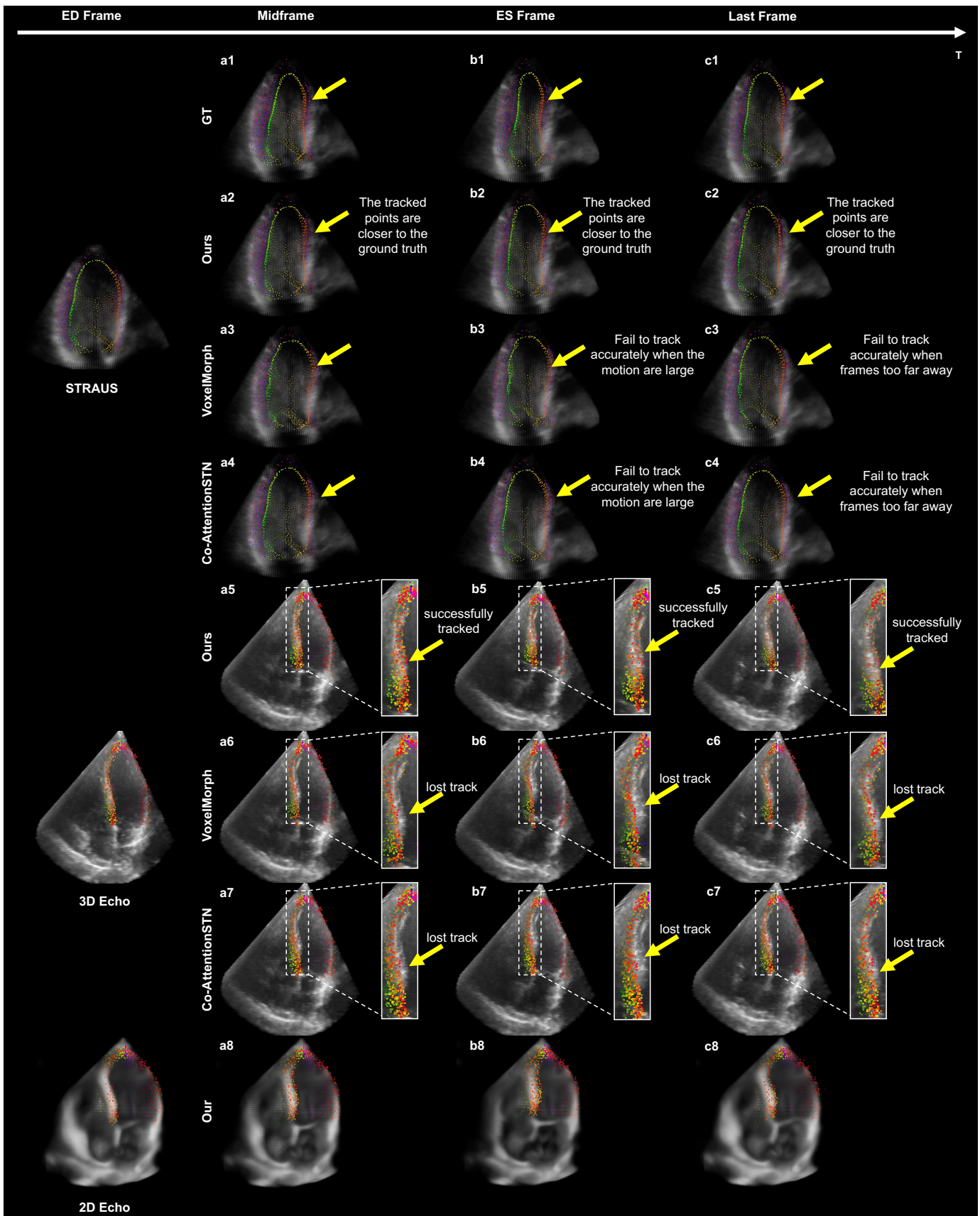


**Fig. 3.** This figure presents the qualitative results of point tracking using our method, VoxelMorph, and Co-AttentionSTN on the STRAUS, 2D, and 3D echocardiogram video datasets. The query points that need to be tracked during the end-diastole (ED) phase are displayed in the first column. The following three columns visually demonstrate the movement of these points across the full cardiac cycle. In the 2D echocardiogram video datasets, only our results are showcased since other methods are incompatible with 2D datasets.

wall. Importantly, this dataset is accompanied by ground truth motion vectors, which have been derived from the movement of the left ventricular (LV) mesh. These vectors are instrumental in modeling the heart’s motion, providing a valuable reference for analyzing and validating computational approaches. The 3D video in each data has a resolution  $224 \times 176 \times 208$  with 34 frames. This comprehensive dataset facilitates a robust examination of various heart conditions and serves as a valuable resource for analyzing and validating cardiac motion modeling.

2) *2D and 3D Echocardiogram Video Datasets*: This dataset [39] contains 56 video pairs from different volunteers. Each pair consists of 2D and corresponding 3D videos for the same volunteer. The 2D echocardiogram video dataset was acquired using commercial PHILIPS EPIQ 7C/IE ELITE machines with S5-1 2DE probes and SIEMENS ACUSON SC2000 PRIME machines with a 4V1c 2DE probe. During the imaging process, sonographers performed 360-degree rotations around the apex of the heart for each individual volunteer. Subsequently, the 2D echocardiogram videos were synchronized based on concurrently recorded ECG signals. Any extraneous elements, such as text, electrocardiogram information, or other unrelated details outside the scanning sector, were cropped and masked. The images were subsequently resized to  $160 \times 160$ -pixel dimensions utilizing a bicubic interpolation filter. In addition to the 2D videos, the 3D echocardiogram video dataset was acquired for each volunteer using commercial PHILIPS EPIQ 7C machines equipped with a X5-1 3DE probe. These 3D images were captured employing a standard four-chamber apical view.

## B. Implementation Details

The proposed NeuralCMF is implemented using the PyTorch framework. We use the FusedAdam optimizer, which is an implementation of the Adam optimizer [44] that fuses multiple CUDA kernels and uses half-precision arithmetic to improve GPU memory usage and performance. The learning rate, initialized as 0.0001, is decayed according to the cosine annealing schedule. We trained our model for  $10^6$  iterations with 8192 points sampled in each iteration, and  $\alpha_1 = \alpha_2 = 0.1$ ,  $\alpha_r = 0.01$ . For every individual point, the position coordinate  $\vec{X}$  is normalized to the range  $[0, 1]$ . The time  $t$  is subjected to repetition with the period of the cardiac cycle to align our implementation with the cyclic nature of the heartbeat,

$$t_{norm} = \frac{t \bmod T}{T}. \quad (12)$$

For both the STRAUS dataset and the 3D echocardiogram video dataset, NeuralCMF is designed to take 3D video sequences as input. We sample the dataset, extracting 4 images per cardiac cycle. With regard to the 2D echocardiogram video datasets, NeuralCMF takes the 2D images as input, and our model processes 200 different view sequences.

## C. Results

1) *Evaluation Metrics*: The experimental investigations conducted on the STRAUS dataset were evaluated using the

provided ground-truth motion vectors. This facilitated the calculation of two key metrics: the median tracking error (MTE) and the cosine similarity. The MTE metric, determined by the  $\mathcal{L}_2$ -norm between the ground truth and predicted motion vectors, evaluates the quantitative accuracy of the tracking, while the cosine similarity serves as a measure of the alignment of the directional components of the motion vectors, with 1 signifying perfect alignment and -1 indicating completely opposite directions. Together, these metrics provide a comprehensive evaluation of both the magnitude and direction of the computed motion fields.

In the case of the 2D and 3D echocardiogram video datasets [39], where ground-truth motion vectors are unavailable, we relied on segmentation-based assessments. We employ metrics such as the Hausdorff Distance (HD), Dice Similarity Coefficient and Jaccard Index, comparing them against provided segmentation masks across two phases. The segmentation masks are labeled by an experienced echosonographer. Using the learned motion vectors, we warped the 3D images from the end-diastolic (ED) phase to the end-systolic (ES) phase. Subsequently, we compared the myocardium segmentation of the LV in the four-chamber apical view from the warped ES phase to the myocardium segmentation in the real ES phase.

The NeuralCMF is evaluated against various state-of-the-art registration/motion tracking algorithms across each dataset for a robust quantitative comparison. Specific comparisons were made with other deep learning-based methods, including VoxelMorph [20] and Co-AttentionSTN [19]. An ablation study was also included to assess the incremental benefit of our proposed cardiac cycle loss. We further compared the running time for motion estimation among our method, VoxelMorph, and Co-AttentionSTN to demonstrate the superiority of our approach.

2) *Results on STRAUS and 3D Echocardiogram Video Datasets*: In Table I, we offer quantitative comparisons of our proposed method using the STRAUS and the 3D Echocardiogram video datasets. Against competitors like VoxelMorph and Co-AttentionSTN, our method persistently outperforms in all evaluation metrics. The results from the 3D Echocardiogram Video Datasets are lower than those from the STRAUS datasets. This discrepancy can be attributed to the higher signal-to-noise ratio present in the STRAUS datasets compared to the 3D Echocardiogram Video Datasets. Figure 3 illustrates the tracking results for both the STRAUS and 3D datasets. The images of LV myocardium at different frames are displayed from left to right. In the leftmost image, a total of 2500 points from the myocardium are selected and colored. Then, the corresponding points obtained by different motion tracking algorithms are plotted in the right 3 images. NeuralCMF demonstrates robust and consistent tracking capabilities throughout the cardiac cycle. Specifically, within the STRAUS datasets, tracking points transition from the ED to the ES phase (representing the largest movement in the cardiac cycle). There are two problems in tracking results of VoxelMorph and Co-AttentionSTN. First, the estimated motion displacement is shorter than the ground truth. The range of colored tracking points on the endocardium appears to be larger than the ground truth, as indicated by the yellow arrow in Fig. 3b1-b4. Second,

TABLE I

QUANTITATIVE COMPARISONS ON STRAUS, 2D, AND 3D ECHOCARDIOGRAM VIDEO DATASETS. FOR BOTH THE 3D AND 2D ECHOCARDIOGRAM VIDEO DATASETS, THE GROUND TRUTH MOTION IS UNAVAILABLE, MAKING IT IMPOSSIBLE TO COMPUTE THE MTE AND COSINE SIMILARITY. IN THE 2D ECHOCARDIOGRAM VIDEO DATASETS, ONLY OUR RESULTS ARE SHOWCASED SINCE OTHER METHODS ARE INCOMPATIBLE WITH 2D DATASETS.

Datasets	Methods	Median tracking error (mm) ↓	Cosine similarity ↑	DICE ↑	HD (mm) ↓	Jaccard index ↑
STRAUS	VoxelMorph [20]	$3.72 \pm 0.32$	$0.68 \pm 0.04$	$0.74 \pm 0.05$	$3.08 \pm 0.12$	$0.58 \pm 0.06$
	Co-AttentionSTN [19]	$4.41 \pm 0.48$	$0.69 \pm 0.08$	$0.71 \pm 0.04$	$3.30 \pm 0.10$	$0.56 \pm 0.05$
	Ours (w/o. $\mathcal{L}_{motion}$ , $\mathcal{L}_{cycle}$ )	fail to converge	fail to converge	fail to converge	fail to converge	fail to converge
	Ours (w/o. $\mathcal{L}_{cycle}$ )	$3.00 \pm 0.07$	$0.76 \pm 0.02$	$0.79 \pm 0.01$	$3.02 \pm 0.01$	$0.67 \pm 0.02$
	Ours	<b><math>2.88 \pm 0.10</math></b>	<b><math>0.78 \pm 0.02</math></b>	<b><math>0.82 \pm 0.02</math></b>	<b><math>3.02 \pm 0.01</math></b>	<b><math>0.69 \pm 0.03</math></b>
3D Echo	VoxelMorph [20]	-	-	$0.62 \pm 0.10$	$3.48 \pm 0.23$	$0.45 \pm 0.10$
	Co-AttentionSTN [19]	-	-	$0.58 \pm 0.07$	$3.42 \pm 0.31$	$0.42 \pm 0.07$
	Ours	-	-	<b><math>0.69 \pm 0.06</math></b>	<b><math>3.25 \pm 0.47</math></b>	<b><math>0.53 \pm 0.07</math></b>
2D Echo	Ours	-	-	<b><math>0.68 \pm 0.07</math></b>	<b><math>4.86 \pm 0.6</math></b>	<b><math>0.52 \pm 0.08</math></b>

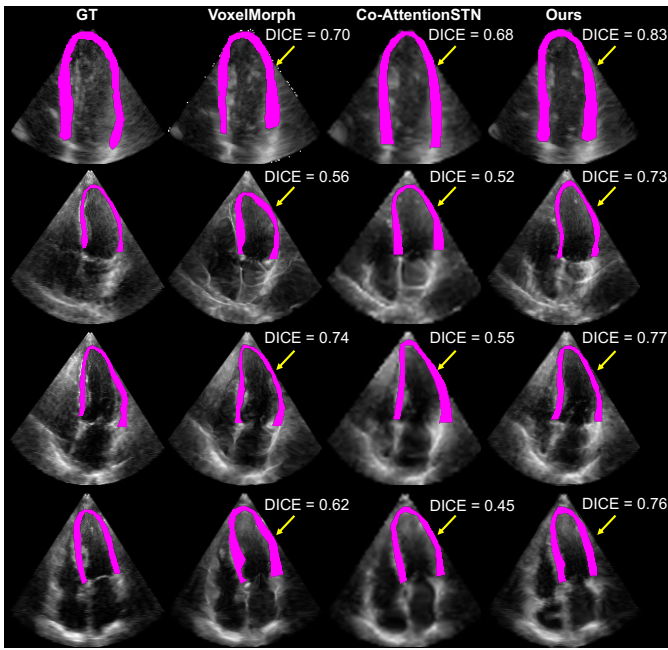


Fig. 4. This experiment demonstrates that our model offers a more precise motion estimation, with the warped image aligning closely to the actual physiological structure of the heart. The figure illustrates a comparison of our warped image results with those obtained using other deep-learning-based methods. The warping process involves taking a 3D image at the end-diastolic (ED) phase and transforming it with estimated displacements to create corresponding 3D images at the end-systolic (ES) phase. Subsequently, we slice the apical four-chamber view for a detailed comparison. For clarity, the left ventricular (LV) myocardium is segmented, and the DICE index is computed between the ground truth and warped ES phase images.

points on the endocardium, which are uniformly sampled in the ED phase, become non-uniform in the ES phase as shown in Fig. 3b3, resulting in a loss tracking of starting points. In contrast, our method aligns myocardium points with the ground truth more precisely than these competing methods.

Regarding the 3D Echocardiogram video datasets, our approach consistently maintains tracking of the point as the myocardium transitions from ED to ES. Conversely, other methods frequently exhibit tracking inconsistencies, leading to point misplacement or loss during this critical stage. As illustrated in Fig. 3b6 and b7, both VoxelMorph and Co-AttentionSTN fail to track points on the interventricular septum (as indicated by the yellow arrow) during the ES phase. Particularly when myocardium movements are more substan-

tial than in the ED phase, VoxelMorph and Co-AttentionSTN tend to lose track. Our method, however, reliably monitors these points across the entire cardiac cycle. Additionally, as shown in Fig. 3c5 - c7, our method outperforms VoxelMorph and Co-AttentionSTN in tracking myocardium movement, even over prolonged durations. This superiority is evident in the last frame of Fig. 3, where our method continues to track the interventricular septum accurately, whereas VoxelMorph and Co-AttentionSTN both lose their tracking points.

The comparison in Fig. 4 indicates that our model produces results that align more precisely with the heart's actual structure. Figure 4 offers visual comparisons on the results of the warping process applied to 3D images. Specifically, the 3D images at the end-diastolic (ED) phase are transformed using the estimated motion vectors to create corresponding 3D images at the end-systolic (ES) phase. We then slice the apical four-chamber view from this 3D model for a detailed comparison. To offer a clearer comparison, we segment the myocardium of the LV and compute the DICE index between the ground truth and the warped images at the ES phase. Notably, the DICE score of our method surpasses that of other methods.

3) *Results on 2D Echocardiogram Video Datasets:* Our proposed method demonstrates adaptability capable of accurately estimating 3D motion from both 3D echocardiogram videos and multi-view 2D images. This multi-functionality is not restricted to mere motion estimation; our model is also capable of reconstructing a dynamic heart from 2D images concurrently, highlighting its capacity for handling multiple tasks simultaneously. The performance of our approach is validated through a comprehensive assessment that includes both quantitative and qualitative evaluations. The motion estimation results of 2D Echocardiogram Video Datasets are thoroughly detailed in Table I, offering a statistical insight into the model's precision and consistency in tracking motion. Figure 3 visually represents the point tracking results, enabling a more intuitive understanding of the method's effectiveness across cardiac cycles. Additionally, our model's ability to reconstruct the 3D dynamic heart is evaluated by comparing its reconstruction results with CardiacField and the 3D hearts captured using a 3DE probe, as illustrated in Fig. 5. Compared to the 3DE probe, the 3D heart structure represented by both the CardiacField and our approach closely aligns with that of the 3DE probe. Moreover, both the CardiacField and our



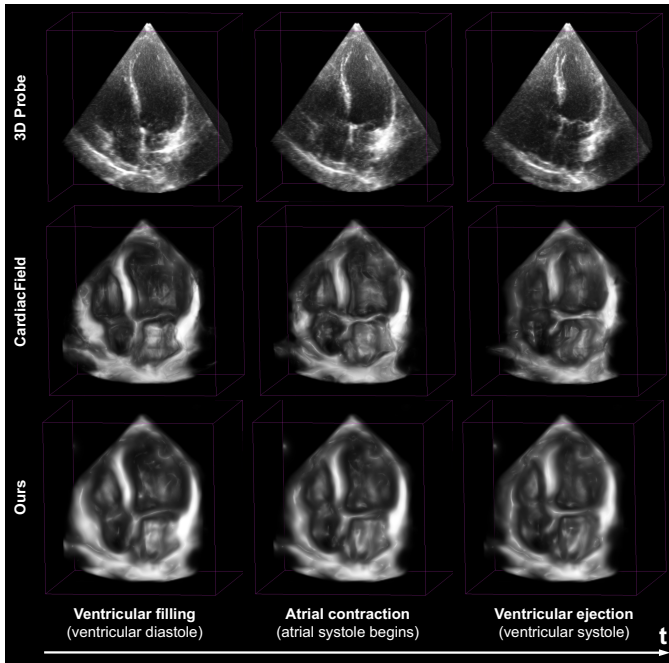


Fig. 5. We show snapshots of a reconstructed 3D dynamic heart within one cardiac cycle using our proposed method, and compare these with the outputs from CardiacField and images acquired via the 3DE probe.

results exhibit a superior signal-to-noise ratio than the 3DE probe. Notably, our method displays less noise compared to the CardiacField. This reduction in noise may be attributed to the incorporation of the physical motion consistency loss and the physical cardiac cycle consistency loss in NeuralCMF. It ensures that the intensity of each point in the 3D heart remains consistent throughout the cardiac cycle. This experiment validates the multitasking ability of our method, demonstrating its robustness in handling complex cardiac imaging tasks.

4) *Ablation Study*: In order to deeply understand each component within our loss function, we conducted a series of ablation studies. These studies analyzed the influence of different components, with the performance metrics present in Table I. Our analysis reveals that the model cannot be optimized without physical motion consistency loss  $\mathcal{L}_{motion}$  and physical cardiac cycle consistency loss  $\mathcal{L}_{cycle}$ . This emphasizes the crucial importance of physical loss we proposed in stabilizing the learning process and ensuring convergence to a solution. Additionally, we observed a decline in model performance without physical cardiac cycle consistency loss  $\mathcal{L}_{cycle}$ . More importantly, the absence of this loss led to instability within the optimization process, further underlining its significance in the model’s architecture.

#### D. Complexity

Table II presents the running time of our method in comparison to VoxelMorph and Co-AttentionSTN using a single Nvidia A100 GPU with 40GB memory. Our method stands out in its efficiency: we do not require paired training data, thus circumventing the need for model pre-training and the accumulation of vast datasets. Such efficiency not only expedites processes of motion estimation but also implies potential cost and resource savings, particularly vital in clinical diagnosis settings where time and precision are paramount.

TABLE II

COMPARISON OF RUNNING TIMES (IN MINUTES) FOR MOTION ESTIMATION OF AN INDIVIDUAL ON THE STRAUS DATASET.

Methods	Pre-Training	Motion Estimation	Overall
VoxelMorph [20]	54.55	0.24	54.79
Co-AttentionSTN [19]	94.13	<b>0.08</b>	94.21
Ours	<b>0</b>	8.58	<b>8.58</b>

## V. DISCUSSION AND CONCLUSION

The diagnostic, prognostic, and preventive measures associated with CVDs remain critical clinical concerns. Given the ubiquity of echocardiography as a bedside imaging modality, its precision in monitoring myocardial movement is vital for identifying abnormalities in the heart. In this context, we introduce the Neural Cardiac Motion Field (NeuralCMF), which is a self-supervised algorithm for modelling cardiac structures and delineating myocardial dynamics.

Traditional approaches, whether speckle-based or surface-based, face intrinsic limitations. The former face challenges in tracking extended temporal frames, while the latter must contend with interpolative inaccuracies, especially evident in non-uniform myocardium movement cases. NeuralCMF overcomes these challenges, providing a holistic view of cardiac motion rather than a frame-by-frame analysis. The burgeoning field of deep learning, while transformative, presents challenges, especially in data dependency. However, our NeuralCMF does not need extensive paired datasets. The incorporation of a physics-informed self-supervision mechanism not only amplifies its accuracy but also broadens its scope of applicability. One of the remarkable features of NeuralCMF is its adaptability. The model accurately estimates myocardial motion when interpreting 2D or 3D echocardiogram videos or dealing with varied resolutions. Such adaptability, particularly its capacity to integrate with different imaging modalities, makes it a valuable tool for researchers and clinicians.

In the future, we’re interested in exploring how our technique might be applied to the non-invasive detection of CVDs, such as coronary heart disease. While this study predominantly focused on cardiac imaging, the underlying techniques have potential applicability beyond the heart. The universality of NeuralCMF offers avenues for exploring other organs and imaging modalities.

## REFERENCES

- [1] A. N. Nowbar, M. Gitto, J. P. Howard, D. P. Francis, and R. Al-Lamee, “Mortality from ischemic heart disease: Analysis of data from the world health organization and coronary artery disease risk factors from ncd risk factor collaboration,” *Circulation: cardiovascular quality and outcomes*, vol. 12, no. 6, p. e005375, 2019.
- [2] C. W. Tsao, A. W. Aday, Z. I. Almarzooq, A. Alonso, A. Z. Beaton, M. S. Bittencourt, A. K. Boehme, A. E. Buxton, A. P. Carson, Y. Commodore-Mensah, *et al.*, “Heart disease and stroke statistics—2022 update: a report from the american heart association,” *Circulation*, vol. 145, no. 8, pp. e153–e639, 2022.
- [3] J. R. Braga, H. Leong-Poi, V. E. Rac, P. C. Austin, H. J. Ross, and D. S. Lee, “Trends in the use of cardiac imaging for patients with heart failure in canada,” *JAMA network open*, vol. 2, no. 8, pp. e198766–e198766, 2019.
- [4] S. Liu, Y. Wang, X. Yang, B. Lei, L. Liu, S. X. Li, D. Ni, and T. Wang, “Deep learning in medical ultrasound analysis: a review,” *Engineering*, vol. 5, no. 2, pp. 261–275, 2019.

- [5] J.-U. Voigt and M. Cvijic, "2-and 3-dimensional myocardial strain in cardiac health and disease," *JACC: Cardiovascular Imaging*, vol. 12, no. 9, pp. 1849–1863, 2019.
- [6] S. Mondillo, M. Galderisi, D. Mele, M. Cameli, V. S. Lomoriello, V. Zacà, P. Ballo, A. D'Andrea, D. Muraru, M. Losi, *et al.*, "Speckle-tracking echocardiography: a new technique for assessing myocardial function," *Journal of Ultrasound in Medicine*, vol. 30, no. 1, pp. 71–83, 2011.
- [7] M. A. Lubinski, S. Y. Emelianov, and M. O'Donnell, "Speckle tracking methods for ultrasonic elasticity imaging using short-time correlation," *IEEE transactions on ultrasonics, ferroelectrics, and frequency control*, vol. 46, no. 1, pp. 82–96, 1999.
- [8] X. Chen, H. Xie, R. Erkamp, K. Kim, C. Jia, J. Rubin, and M. O'Donnell, "3-d correlation-based speckle tracking," *Ultrasonic Imaging*, vol. 27, no. 1, pp. 21–36, 2005.
- [9] X. Papademetris, A. J. Sinusas, D. P. Dione, R. T. Constable, and J. S. Duncan, "Estimation of 3-d left ventricular deformation from medical images using biomechanical models," *IEEE transactions on medical imaging*, vol. 21, no. 7, pp. 786–800, 2002.
- [10] N. Parajuli, A. Lu, K. Ta, J. Stendahl, N. Boutagy, I. Alkhalil, M. Eberle, G.-S. Jeng, M. Zontak, M. O'Donnell, *et al.*, "Flow network tracking for spatiotemporal and periodic point matching: Applied to cardiac motion analysis," *Medical image analysis*, vol. 55, pp. 116–135, 2019.
- [11] X. Huang, D. P. Dione, C. B. Compas, X. Papademetris, B. A. Lin, A. Bregasi, A. J. Sinusas, L. H. Staib, and J. S. Duncan, "Contour tracking in echocardiographic sequences via sparse representation and dictionary learning," *Medical image analysis*, vol. 18, no. 2, pp. 253–271, 2014.
- [12] N. Parajuli, A. Lu, J. C. Stendahl, M. Zontak, N. Boutagy, M. Eberle, I. Alkhalil, M. O'Donnell, A. J. Sinusas, and J. S. Duncan, "Integrated dynamic shape tracking and rf speckle tracking for cardiac motion analysis," in *MICCAI*, pp. 431–438, Springer, 2016.
- [13] P. Shi, A. J. Sinusas, R. T. Constable, E. Ritman, and J. S. Duncan, "Point-tracked quantitative analysis of left ventricular surface motion from 3-d image sequences," *IEEE transactions on medical imaging*, vol. 19, no. 1, pp. 36–50, 2000.
- [14] N. Lin and J. S. Duncan, "Generalized robust point matching using an extended free-form deformation model: application to cardiac images," in *2004 2nd IEEE International Symposium on Biomedical Imaging: Nano to Macro (IEEE Cat No. 04EX821)*, pp. 320–323, IEEE, 2004.
- [15] R. Blankstein and A. H. Waller, "Evaluation of known or suspected cardiac sarcoidosis," *Circulation: Cardiovascular Imaging*, vol. 9, no. 3, p. e000867, 2016.
- [16] A. Ichinose, H. Otani, M. Oikawa, K. Takase, H. Saito, H. Shimokawa, and S. Takahashi, "Mri of cardiac sarcoidosis: basal and subepicardial localization of myocardial lesions and their effect on left ventricular function," *American Journal of Roentgenology*, vol. 191, no. 3, pp. 862–869, 2008.
- [17] S. S. Ahn, K. Ta, A. Lu, J. C. Stendahl, A. J. Sinusas, and J. S. Duncan, "Unsupervised motion tracking of left ventricle in echocardiography," in *Medical imaging 2020: Ultrasonic imaging and tomography*, vol. 11319, pp. 196–202, SPIE, 2020.
- [18] K. Ta, S. S. Ahn, J. C. Stendahl, A. J. Sinusas, and J. S. Duncan, "A semi-supervised joint network for simultaneous left ventricular motion tracking and segmentation in 4d echocardiography," in *MICCAI*, pp. 468–477, Springer, 2020.
- [19] S. S. Ahn, K. Ta, S. L. Thorn, J. A. Onofrey, I. H. Melvinsdottir, S. Lee, J. Langdon, A. J. Sinusas, and J. S. Duncan, "Co-attention spatial transformer network for unsupervised motion tracking and cardiac strain analysis in 3d echocardiography," *Medical Image Analysis*, vol. 84, p. 102711, 2023.
- [20] G. Balakrishnan, A. Zhao, M. R. Sabuncu, J. Guttag, and A. V. Dalca, "Voxelmorph: a learning framework for deformable medical image registration," *IEEE transactions on medical imaging*, vol. 38, no. 8, pp. 1788–1800, 2019.
- [21] P. J. Besl and N. D. McKay, "Method for registration of 3-d shapes," in *Sensor fusion IV: control paradigms and data structures*, vol. 1611, pp. 586–606, Spie, 1992.
- [22] H. Chui and A. Rangarajan, "A new point matching algorithm for non-rigid registration," *Computer Vision and Image Understanding*, vol. 89, no. 2-3, pp. 114–141, 2003.
- [23] M.-M. Rohé, M. Datar, T. Heimann, M. Sermesant, and X. Pennec, "Svfnet: learning deformable image registration using shape matching," in *MICCAI*, pp. 266–274, Springer, 2017.
- [24] J. Wu, T. R. Mazur, S. Ruan, C. Lian, N. Daniel, H. Lashmett, L. Ochoa, I. Zoberi, M. A. Anastasio, H. M. Gach, *et al.*, "A deep boltzmann machine-driven level set method for heart motion tracking using cine mri images," *Medical image analysis*, vol. 47, pp. 68–80, 2018.
- [25] O. Ronneberger, P. Fischer, and T. Brox, "U-net: Convolutional networks for biomedical image segmentation," in *MICCAI*, pp. 234–241, Springer, 2015.
- [26] H. Yu, S. Sun, H. Yu, X. Chen, H. Shi, T. S. Huang, and T. Chen, "Foal: Fast online adaptive learning for cardiac motion estimation," in *IEEE CVPR*, pp. 4313–4323, 2020.
- [27] H. Yu, X. Chen, H. Shi, T. Chen, T. S. Huang, and S. Sun, "Motion pyramid networks for accurate and efficient cardiac motion estimation," in *MICCAI*, pp. 436–446, Springer, 2020.
- [28] V. Sitzmann, J. Martel, A. Bergman, D. Lindell, and G. Wetzstein, "Implicit neural representations with periodic activation functions," *NeurIPS*, vol. 33, pp. 7462–7473, 2020.
- [29] B. Mildenhall, P. P. Srinivasan, M. Tancik, J. T. Barron, R. Ramamoorthi, and R. Ng, "Nerf: Representing scenes as neural radiance fields for view synthesis," *Communications of the ACM*, vol. 65, no. 1, pp. 99–106, 2021.
- [30] K. He, X. Zhang, S. Ren, and J. Sun, "Deep residual learning for image recognition," in *IEEE CVPR*, pp. 770–778, 2016.
- [31] J. Zhu, H. Zhu, Q. Zhang, F. Zhu, Z. Ma, and X. Cao, "Pyramid nerf: Frequency guided fast radiance field optimization," *International Journal of Computer Vision*, pp. 1–16, 2023.
- [32] R. Liu, Y. Sun, J. Zhu, L. Tian, and U. S. Kamilov, "Recovery of continuous 3d refractive index maps from discrete intensity-only measurements using neural fields," *Nature Machine Intelligence*, vol. 4, no. 9, pp. 781–791, 2022.
- [33] H. Zhu, Z. Liu, Y. Zhou, Z. Ma, and X. Cao, "Dnf: diffractive neural field for lensless microscopic imaging," *Optics Express*, vol. 30, no. 11, pp. 18168–18178, 2022.
- [34] Y. Chen, L. Lu, G. E. Karniadakis, and L. Dal Negro, "Physics-informed neural networks for inverse problems in nano-optics and metamaterials," *Optics express*, vol. 28, no. 8, pp. 11618–11633, 2020.
- [35] G. E. Karniadakis, I. G. Kevrekidis, L. Lu, P. Perdikaris, S. Wang, and L. Yang, "Physics-informed machine learning," *Nature Reviews Physics*, vol. 3, no. 6, pp. 422–440, 2021.
- [36] L. Shen, J. Pauly, and L. Xing, "Nerp: implicit neural representation learning with prior embedding for sparsely sampled image reconstruction," *IEEE Transactions on Neural Networks and Learning Systems*, 2022.
- [37] R. Zha, Y. Zhang, and H. Li, "Naf: neural attenuation fields for sparse-view cbct reconstruction," in *MICCAI*, pp. 442–452, Springer, 2022.
- [38] Q. Wu, Y. Li, Y. Sun, Y. Zhou, H. Wei, J. Yu, and Y. Zhang, "An arbitrary scale super-resolution approach for 3d mr images via implicit neural representation," *IEEE Journal of Biomedical and Health Informatics*, vol. 27, no. 2, pp. 1004–1015, 2022.
- [39] C. Shen, H. Zhu, Y. Zhou, Y. Liu, S. Yi, L. Dong, W. Zhao, D. Brady, X. Cao, Z. Ma, and Y. Lin, "Cardiacfield: Computational echocardiography for universal screening," *Research Square*, 2023.
- [40] T. Müller, A. Evans, C. Schied, and A. Keller, "Instant neural graphics primitives with a multiresolution hash encoding," *ACM Transactions on Graphics (ToG)*, vol. 41, no. 4, pp. 1–15, 2022.
- [41] S. Xie, H. Zhu, Z. Liu, Q. Zhang, Y. Zhou, X. Cao, and Z. Ma, "DINER: Disorder-invariant implicit neural representation," in *IEEE CVPR*, pp. 1–10, 2023.
- [42] M. De Craene, G. Piella, O. Camara, N. Duchateau, E. Silva, A. Doltra, J. D'hooge, J. Brugada, M. Sitges, and A. F. Frangi, "Temporal diffeomorphic free-form deformation: Application to motion and strain estimation from 3d echocardiography," *Medical image analysis*, vol. 16, no. 2, pp. 427–450, 2012.
- [43] M. Alessandrini, M. De Craene, O. Bernard, S. Giffard-Roisin, P. Allain, I. Waechter-Stehle, J. Weese, E. Saloux, H. Delingette, M. Sermesant, *et al.*, "A pipeline for the generation of realistic 3d synthetic echocardiographic sequences: Methodology and open-access database," *IEEE transactions on medical imaging*, vol. 34, no. 7, pp. 1436–1451, 2015.
- [44] D. P. Kingma and J. Ba, "Adam: A method for stochastic optimization," *arXiv preprint arXiv:1412.6980*, 2014.